Towards 3D-Electrical Capacitance Tomography for interface detection

Clark, Peter; Forte, Giuseppe; Simmons, Mark; Stitt, E. Hugh

[Link to publication on Research at Birmingham portal](#)

Towards 3D-Electrical Capacitance Tomography for interface detection

P. J. Clark[a,b,*], G. Forte [a,b], M. J. H. Simmons[b], E. H. Stitt[a]

[a] *Johnson Matthey Technology Centre, Billingham, UK, TS23 1LB*
[b] *School of Chemical Engineering, University of Birmingham, Edgbaston, UK, B15 2TT*
* Corresponding author: peter.clark@matthey.com

Keywords: interface, capacitance, tomography, 3D

Abstract

The application of 3-dimensional Electrical Capacitance Tomography (3D-ECT) for the *in-situ* monitoring of a hard boundary/interface has been investigated using imaged phantoms that simulate real-life processes. A cylinder-in-tube phantom manufactured from polyethylene (PE), a low di-electric and non-conductive material, was imaged using the linear back projection (LBP) algorithm with the larger tube immersed at varying intervals to test the ability of the technique to image interfaces axially through the sensor. The interface between PE and air is clearly imaged and correlates to the known tube penetration within the sensor. The cylinder phantom is imaged in the centre of the sensor, however, the reduction in measurement density towards the centre of the ECT sensor results in reduced accuracy. A thresholding method, previously applied to binary systems to improve the imaged accuracy of a hard boundary between two separate phases, has been applied to the 3D-ECT tomograms that represent the PE phantom. This approach has been shown to improve the accuracy of the acquired image of a cylinder of air within a non-conductive PE tube.

1.0. *Introduction*

The ability to accurately and quickly monitor the evolution of physical and chemical changes within products during manufacturing has been the subject of much interest in both academic and industrial research communities. Enhanced process monitoring allows an engineer to implement better control thereby increasing efficiency, improving material and energy usage and increasing product quality. Electrical tomography has been developed over the last few decades with the purpose of delivering real time, *in-situ* measurements of phase distributions within a process vessel or pipe. It provides spatially resolved information on the distribution of material properties (permittivity, conductivity, density) within a cross-sectional plane through the sensing zone represented by a pixel grid known as a tomogram. In the majority of cases to date 2D images have been sufficient to provide the required process information for the user, however, 3D tomography provides spatial information in both radial and axial planes yielding greater process insight. The compromise when applying 3D methods as opposed to 2D is increased computing time, greater complexity of hardware and requirement for advanced reconstruction algorithms.

Electrical tomography is categorised as a soft-field method. The distribution of the electric field within the sensor is unknown thus forming a non-linear relationship between the measured capacitances at the boundary of the sensor and the material distribution within the sensor, hence the term 'soft-field'. Electrical Capacitance Tomography (ECT) is a specific form of electrical tomography applicable to systems with a non-conductive continuum and an insulating process vessel wall. It utilises a concentric ring of uniformly spaced electrodes fixed to the outside of a non-conductive vessel wall. The signal-to-noise ratio (SNR) of the system is dependent upon the area of each electrode therefore studies have been conducted that determine the optimal size of ECT electrodes (1). Guard electrodes are also required to prevent process materials outside the sensing zone having an effect upon the electric field

distribution (2). The number of electrodes used within the sensor ring is a compromise between the required size of electrode to deliver the required SNR, the diameter of the electrode array (directly related to the diameter of the process vessel) and the desired reconstructed image accuracy with a greater number of electrodes delivering increased spatial resolution.

There are two critical parameters when designing an ECT sensor: the ratio of permittivity of continuous and dispersed phases and the thickness of the sensor liner (3). When either of these phases has high relative permittivity there is an increased electrical flux deflection at the boundary of the ECT sensor that results in the relationship between material permittivity and measured capacitance becoming non-linear, typically at relative permittivity values, $\varepsilon_{mat} > 15$. To image these materials a new sensor was developed that applies internal rather than external electrodes to measure the boundary inter-electrode capacitance. This system was used to image an air/de-mineralised water phantom and a water continuous oil-in-water (O/W) dispersion designed to mimic process equipment in the oil industry such as separators and extraction units (3). Whilst the configuration of the sensor solves the boundary linearity problem, it removes the non-intrusive advantage that traditional ECT has over competing methods. In the majority of the process industries it is unlikely that a pipe or unit will be taken offline for electrode fitting, and indeed due to the hazardous nature of the chemicals used any potential for containment risk is unacceptable.

Twin-plane ECT was used to investigate the liquid hold up within a gas/liquid packed bed. Initial measurements using single plane ECT were conducted to determine liquid drainage dynamics and determine its relationship with the gas velocity and packing particle size. Extensive calibrations were performed using twin plane ECT so as to accurately map bed hydrodynamics across the dual sensing zones and the use of tracer led residence time distribution (RTD) combined with ECT analysis to obtain hydrodynamic performance data

was also investigated (4). 3D-ECT has been a controversial topic in recent years due to the similar and often mistakenly applied definitions of 3D and pseudo-3D tomography. Until recently there was a lack of precision hardware and capable software that could obtain full 3D-ECT data, that is to say acquire and reconstruct electrode measurements in the axial, radial and angular dimensions (assuming cylindrical co-ordinates). Prior to suitable commercial equipment being available 2D tomograms were stacked to obtain pseudo-3D images of a process, the term 'pseudo' is used as there are no electrode measurements across the axial plane. A volumetric ECT (ECVT) approach was used to monitor the hydrodynamics of the drying of wet granules with the purpose of being used in the pharmaceutical industry. From the 3D data gained the granule moisture content and drying medium velocity were calculated (5).

The majority of work so far in applied 3D-ECT research has used back-projection approaches for its simplicity, however there has been some work done on a volumetric 3D approach using alternative reconstruction algorithms. A Neural-Network Multi-Criterion Optimisation (NN-MOIRT) algorithm has been developed that effectively applies the optimisation approach across a Hopfield neural network (6). The results have been compared favourably with existing reconstruction algorithms such as the iterative filtered back projection technique (IFPBT) and the iterative linear back projection (ILBP) algorithm. The NN-MOIRT algorithm was then applied to a three phase bubble column so as to image multi-phase flows and showed the enhanced accuracy of this method for 3D-ECT applications (7). The same group then used this approach to complete further work to investigate the dynamics of spiral bubble plume motion in the entrance zone of bubble columns and three-phase fluidised beds (8). The NN-MOIRT approach was again combined with volumetric ECT to investigate a jet of air, issued from a single orifice, within a poppy seed bed of internal diameter 50 mm. The ECVT results were gated to yield optimal images and then compared

directly with MRI data showing consistency at high air flow rates but the ECVT was less sensitive to changes at lower air flow. Standard deviation measurements across the ECVT images gave 7 mm in the radial plane and 8 mm in the axial plane, at least an order of magnitude higher than MRI and confirming ECT as still having significant future work to be considered an accurate imaging technique (9).

ECT has so far been applied to a wide range of engineering processes, however the majority of published work has been done on academic instruments in either single or dual plane configuration. The use of ECT has, in the majority of cases, been restricted to materials with low relative permittivity due to charge saturation effects, a result of electric field non-linearity across the sensor. There is potential for 3D-ECT to be integrated into engineering processes, however, so far there have been few works published using a commercial instrument. This paper addresses this need by applying 3D-ECT to image the mobile interface in a drying packed bed having transient bulk relative permittivity. Firstly, prior work published by the authors is reviewed that presents a method of optimising an image using post-processing techniques and then 3D-ECT is applied to a cylinder-in-tube phantom that simulates a static interface between the phantom and air. Cross-sectional tomograms and 3D iso-surface plots are used to qualitatively assess the system and demonstrate the efficacy of this technique to image an interface.

2.0. *Review of 2D image refinement for high di-electric systems*

ECT has been previously applied for the planar imaging of interfaces in engineering processes typically involving multiphase systems. A common issue with this form of imaging

is that image accuracy is not adequate for a quantitative approach in the analysis. This is due to the resolution of the image which is defined, in this paper, using two terms:

1) Measurement resolution: the distribution of charge measurements governing the sensing zone. This is a function of the number of electrodes within the imaging plane and cannot be affected using post-processing techniques.

2) Image resolution: determined by the chosen reconstruction algorithm and pixel size, both of which can be altered using post-processing.

The authors have previously addressed image refinement of tomograms of high dielectric materials using commercially available ECT equipment (11). The focus of that study was to vary threshold value and optimise the image based upon image error as a function of the threshold. As such two known methods of image error were compared; areal and pixel-by-pixel (PbP). The formulas for these two error functions are given below with PbP given as (1) and the areal analysis given in (2) and (3).

$$e_{PbP} = \frac{100}{N} \sum_{i=1}^{N} \frac{|(\mu_{image} - \mu_{real})|}{\mu_{real}} \tag{1}$$

Where e_{PbP} is the error using the PbP approach, N is the total number of pixels, μ_{image} is the imaged pixel value of pixel i in the tomogram and μ_{real} is the theoretical pixel value of pixel i in the real system. The areal analysis is given below as two stages; the first calculates the area of the image occupied by the phantom:

$$A_{image} = A_C \frac{\sum \mu_{image}}{N} \bigg|_{\mu_{image} < t} \tag{2}$$

Where A_{image} is the area of the image and A_C is the cross-sectional area of the circular sensor chamber. The second stage calculates the error as a ratio of the difference between the areas of the imaged and real object to the area of the real object:

6

$$e_A = \frac{|A_{image} - A_{phantom}|}{A_{phantom}}$$

Where e_A is the image error calculated using the areal approach and $A_{phantom}$ is the area of the phantom. Using these formulae and varying the gate value a correlation can be determined between gate value and image error. The range between threshold values that give an arbitrarily chosen image error dictates the sensitivity of the tomogram accuracy to threshold value.

The experimental approach taken in this work was to image a cylindrical PMMA (poly(methyl-methacrylate)) object within a dual plane ECT sensor with 6" diameter filled with glycerol. The PMMA phantom had relative permittivity of ~2.3 and the glycerol ~40. The phantoms were imaged across a series of frames to check that imaging was reliable and constant, pixel data was then extracted from the tomograms.

(a)

(b)
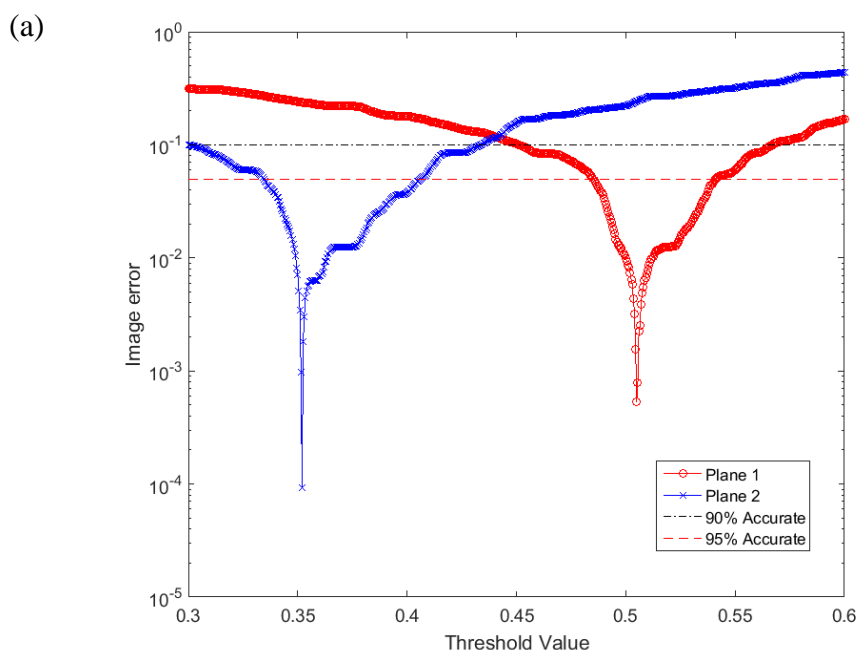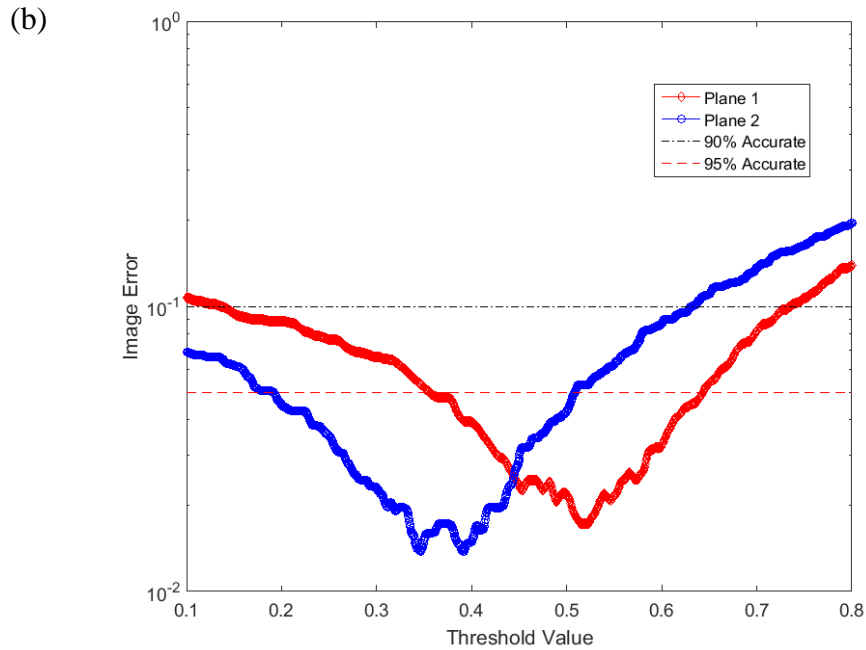
Figure 1 – Image error sensitivity to threshold value for an ECT imaged circular PMMA phantom using (a) Areal and (b) Pixel-by-pixel methods

The optimal threshold value is that which delivers the lowest error value according to the plots shown in Figure 1. The comparison of the areal and pixel-by-pixel approaches given in Figure 1 yields two important results; the optimal threshold values calculated using each method are consistent demonstrating robustness and the calculated image error using the areal approach is much lower as it is not constrained to the pixel resolution. It is important to note that the optimal threshold value can only be used when imaging a system with identical physical properties i.e. continuum and dispersed phase must have identical electrical properties to that used to obtain the optimal threshold value.
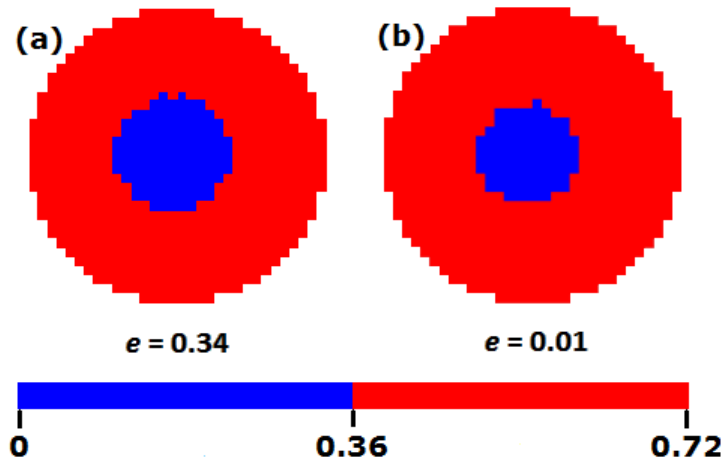
Figure 2 - Binary tomograms of circular PMMA phantom for plane 2 (a) threshold = 0.5 (b) threshold = 0.36. The given error value, e, was calculated using the pixel-by-pixel method

Applying the optimal threshold value determined in Figure 1 to the acquired tomograms gives an optimised image that better represents the real system/phantom. In Figure 2 this is clearly shown to reduce the area occupied by the imaged phantom therefore the original image was over-sized, a result of poor reconstruction using the LBP algorithm. The binary image shows the location of the interface by its very definition and therefore by optimising the image the interface has been more accurately imaged also. However, as Figure 2 also clearly shows, any accurate measurements of the interface are dependent upon pixel resolution which, in this case, is poor.

This work has shown that post-processing techniques can be used to successfully optimise 2D-ECT images, primarily for the purposes of imaging interfaces. There were two directions future work could progress; the first is 3D-ECT which is explored further in this paper, and the second is in better reconstruction algorithms that yield higher resolution images without the need for interpolation. The latter option is the intent of many academic studies but is not currently commercialised and is therefore not an option for a tomography user.

3.0. *Materials and Methods for 3D-ECT imaging*

The objectives of this work were to determine the usefulness of ECT as an online measurement tool for interface detection within a three-dimensional sensing zone using materials of high relative permittivity and to investigate the capability of a commercially available ECT instrument to deliver 3D images of a transient system including an evolving interface. The separate experiments are described below.
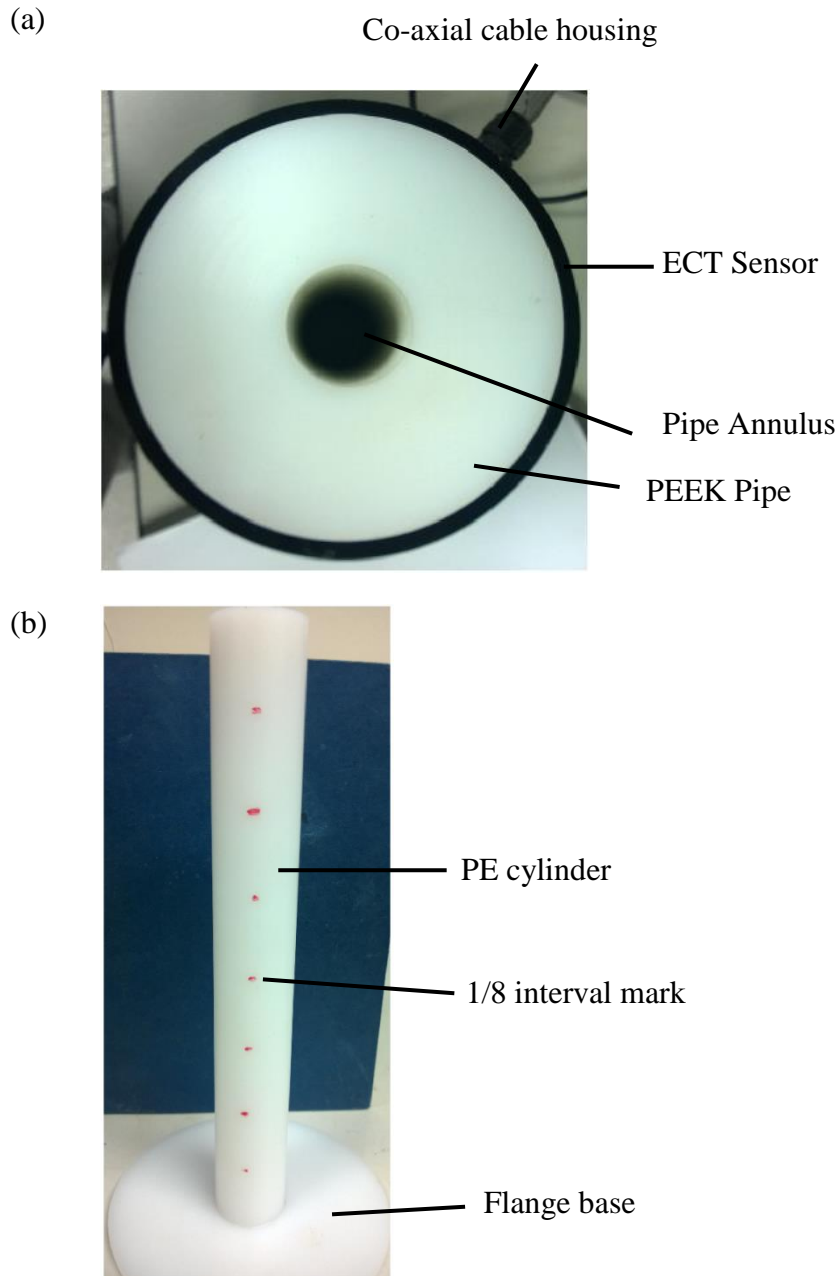
3.1. Cylinder-in-tube phantom configuration

In order to show the development of a hard interface in the radial plane moving axially through the sensor a series of phantom experiments were designed. Phantoms are objects of known dimensions that simulate/mimic a desired process or system. A triple plane ECT sensor was used comprising of a polyether ether ketone (PEEK) cylinder of inner diameter of 156 mm with 3 planes of 8 electrodes implanted to the outside of the wall and encased in stainless steel. A cylinder-in-tube polyethylene (PE) phantom was used to simulate the interface. The PE tube had diameter 142 mm with an annular core of diameter 30 mm, tube wall thickness of 62 mm and was 300 mm long. The PE cylinder was 30 mm in diameter and 300 mm long with a flanged base having a diameter of 160 mm. The schematics for these phantoms are given in Figure 3.

(a)

160 mm

140 mm

40 mm

300 mm

(b)

160 mm

40 mm

300 mm
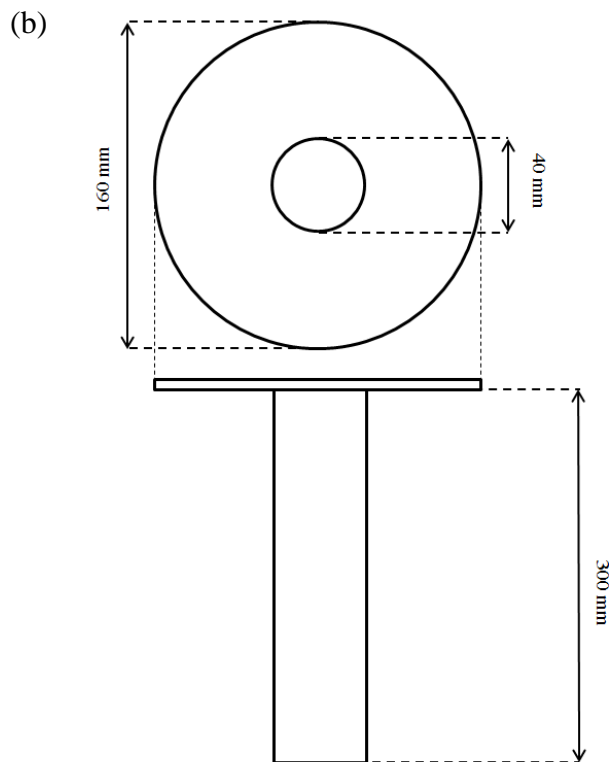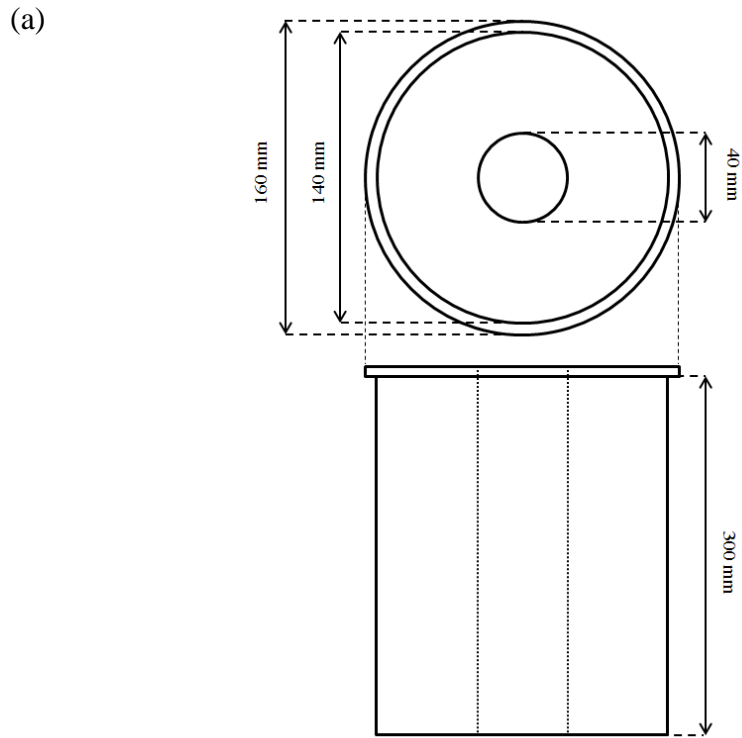
Figure 3 - Schematics for cylinder-in-tube phantom experiments (a) Thick-walled PE tube showing annulus, (b) PE cylinder with flange base

The small cylinder (Figure 3(b)) and sensor were raised above the large tube (Figure 3(a)) and imaged at penetration intervals of 1/8 of the length of the small cylinder. Once the whole of the large tube had been removed, the sensor was imaging just the small cylinder with a large air gap between the sensor wall and the phantom. The 1/8 penetration intervals were measured and marked onto the polyethylene cylinder shown in Figure 4(b).

(a)

(b)

Figure 4 – Individual components of cylinder-in-tube phantom (a) Thick-walled PE tube within PEEK-lined ECT sensor, (b) PE 40 mm diameter cylinder with flanged base

Figure 4(a) shows the large tube housed within the PEEK-lined ECT sensor. There is an air gap of 1 mm between the PE large tube and the wall of the sensor. As this is present during the sensor calibration it has no impact on the reconstructed ECT data. The 1/8 intervals of the length of the small cylinder that the large tube was imaged at are shown in Figure 4(b) as markings on the small cylinder.

3.2. ECT Setup and Configuration

The ECT instrument used for this work was an Industrial Tomography Systems (ITS) m3c 24 input channel unit. Individual electrodes were connected from the sensor to the instrument ports using BNC cables. The first step in processing of electrical tomography data is normalisation of the capacitance data according to (4).

$$C_n = \frac{C - C_l}{C_h - C_l} \tag{4}$$

Where C_n and C are the normalised and measured capacitance values respectively, C_h and C_l are capacitance values from the high permittivity and low permittivity reference frames respectively. The reference frames are taken prior to measurement and for both experimental series the conditions for these are given in Table 3-1.

Table 3-1 - High and low permittivity reference frames - material properties for both phantom and drying bed experimental series, ε_r = Relative permittivity

Experimental Series	High Permittivity Reference Frame		Low Permittivity Reference Frame	
	Material	ε_r	Material	ε_r
Phantom	PE	2.2 - 2.4	Air	1.5

The low permittivity reference frame is taken prior to the high permittivity reference frame and once both are acquired process data can be recorded. The phantom experiment was imaged for 30 frames at each interval the large tube was held at thus building a series of images of penetration depth of the small cylinder.

A reconstruction algorithm is required to calculate the spatially resolved material data from electrical boundary measurements. In commercial ECT equipment there has previously been one algorithm available to use, the linear back projection (LBP) algorithm. This assumes a linear relationship between the capacitance and permittivity vectors as given in (5).

$$g = S^T \lambda \tag{5}$$

Where g is the normalised permittivity vector, λ is the normalised capacitance vector and S^T is a linear approximation to the inverse of the sensitivity matrix, S (10). This equation is solved by discretization across a pixel grid containing 1024 pixels that is reduced to 812 pixels as the corners are fileted for circular images. The LBP algorithm is used for image reconstruction of the phantom electrical data.

3.3.   3D-ECT tomogram image processing

A true 3D-ECT measurement acquires charge data in both the radial and axial direction for each stimulus there yielding an output of a 3D tomogram composed of 32x32x32 voxels (corresponding to pixels in three-dimensional space). Each voxel represents a volume portion within the sensor and it assigned a value in the interval between 0 and 1. In order to identify the geometrical shape placed in the sensor, a binary gating method is applied. This method, widely applied in MRI and in 2D-ECT, consists of dividing the tomogram into a number of zones equivalent to the number of phases. In this study one zone

represents the volume occupied by the phantom and the second composed by the surrounding gas phase (11). Once the image has been gated it is possible to compare it with a previously built reference to evaluate the image error. The advantage of using phantoms is that their exact geometry is known and therefore a digitalized reference image as basis for comparison for error analysis is accurate and simple to construct.

The data processing methods applied in the refinement of 2D images have been applied also to the 3D-ECT tomogram analysis. The objective of the gating method is to find the optimum threshold value that allows generation of the binary matrix that describes the object with the minimum error. A reference image has been created to allow the comparison between the reconstructed tomograms and the real object, this image is given below in Figure 5 .
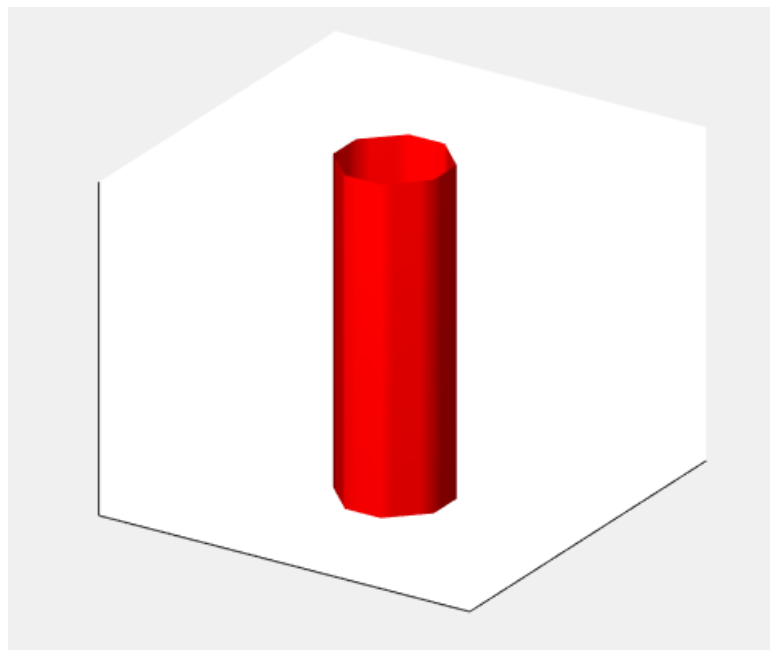
Figure 5 – Pixelated reference image of fully withdrawn PE cylinder from PE tube for comparison in voxel-by-voxel analysis

The pixel-by-pixel approach, defined as voxel-by-voxel in 3D tomography, compares the corresponding voxels in the reconstructed and in the theoretical images (Figure 5) and is described by the same equation as pixel-by-pixel analysis (equation (1)) but in 3D space rather than 2D. The areal approach (equations (2) & (3)) is extended to the third dimension evaluating the volume occupied by the phantom in the image:

$$V_{image} = V_C \frac{\sum \mu_{image}}{N} \Big|_{\mu_{image} < t} \tag{6}$$

Where V_{image} is the volume of the image and V_C is the total volume of the sensor chamber. The volumetric error is calculated evaluating the ratio of the difference between the volumes of the imaged and the real object and the volume of the real object:

$$e_V = \frac{|V_{image} - V_{phantom}|}{V_{phantom}} \tag{7}$$

Where e_V is the image error calculated using the volumetric-areal approach and $V_{phantom}$ is the volume of the phantom.

4.0. *Results and Discussion*

The phantom experiments use PE, with a low relative permittivity, to simulate an interface so the 3D-ECT reconstruction can be trialled using the basic LBP algorithm to ascertain its efficacy before application to high di-electric media. Therefore these experiments are used solely to examine whether 3D-ECT is capable of monitoring an interface.

4.1. 3D ECT Reconstruction using LBP

The ECT three-plane sensor is attached to the flanged base of the small cylinder therefore the phantom is defined as the large tube being inserted into the sensor with the

PE/air interface being the top of the PE large tube. The tomograms are shown below in Figure 6.
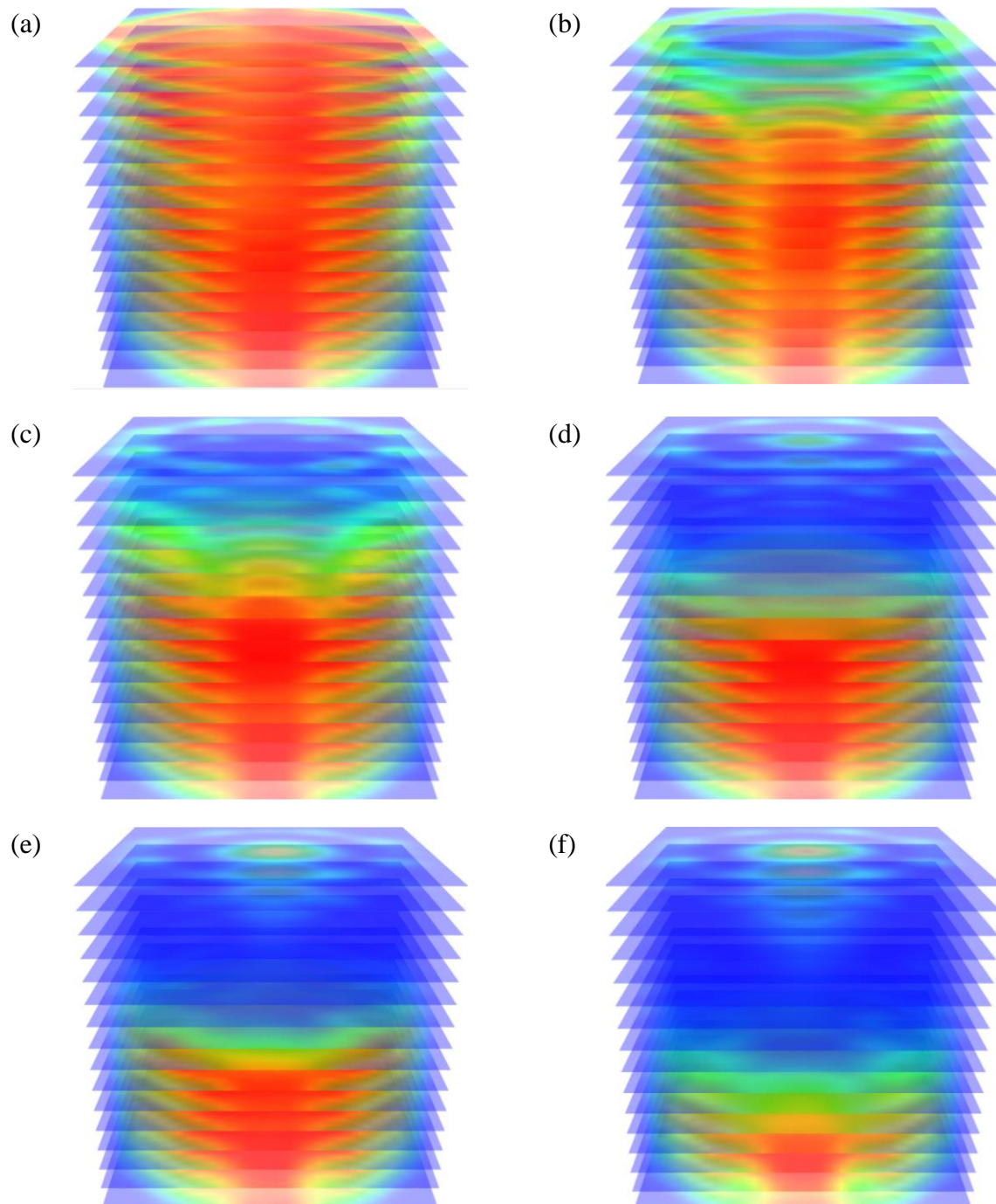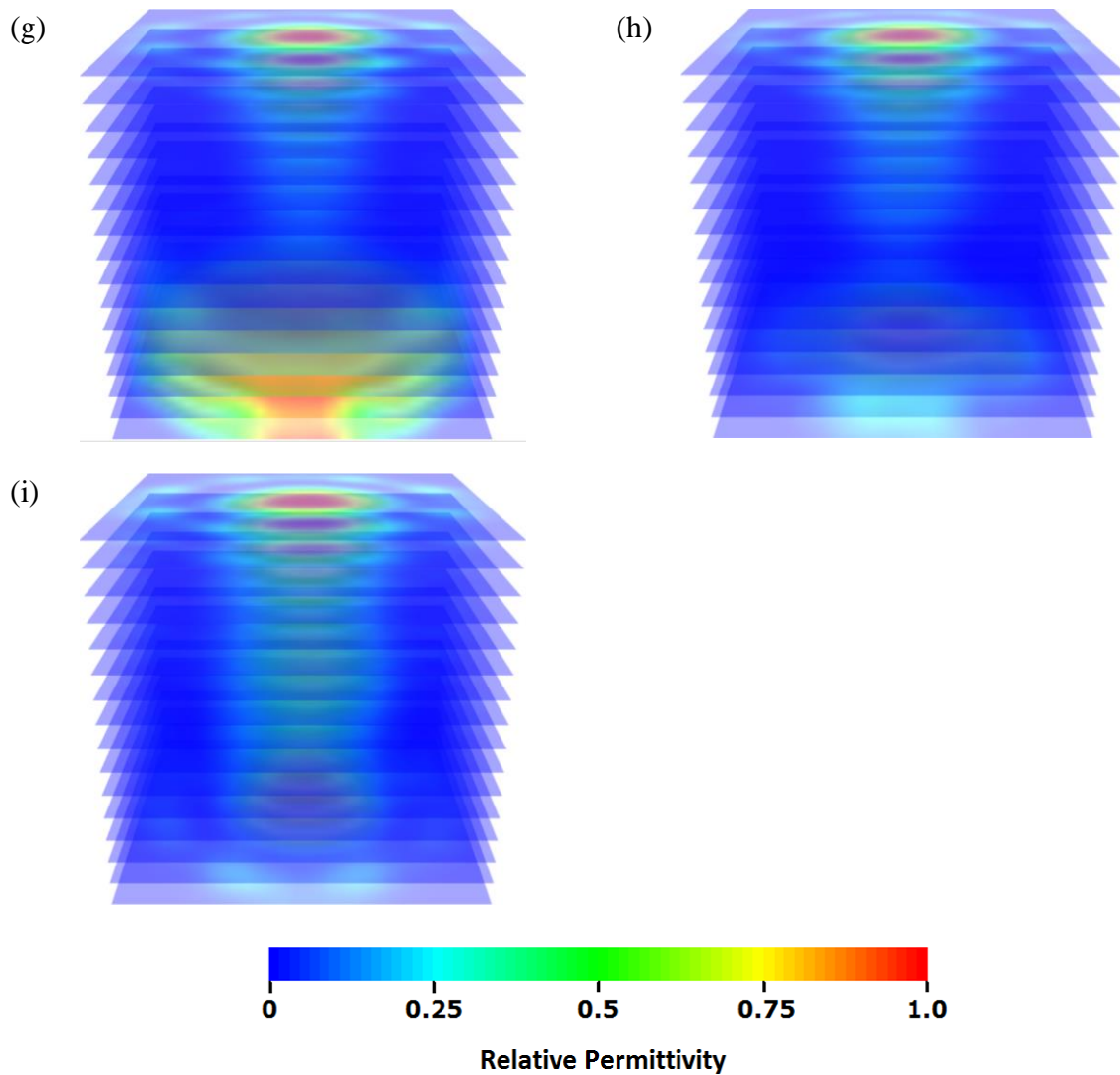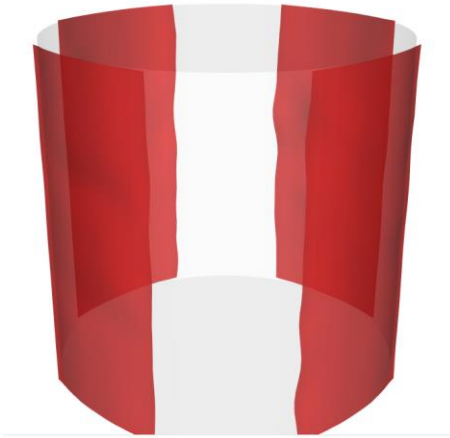
Figure 6 – Cross-section sliced 3D tomograms of cylinder-in-tube phantom experiment, (a) Fully immersed phantom, (b) 7/8 immersed, (c) ¾ immersed, (d) 5/8 immersed, (e) ½ immersed, (f) 3/8 immersed, (g) ¼ immersed, (h) 1/8 immersed, (i) Fully withdrawn

The images displayed in Figure 6 are cross section tomograms whereby the electrode measurements from the 3 planes of uniform electrodes are reconstructed and subsequently discretised to give 16 image planes. In pseudo-3D tomography this form of image is strongly discouraged as the lack of axial inter-electrode capacitance data nullifies any assumptions required to use an inter-plane interpolation approach. This is not the case in 3D-ECT as inter-electrode capacitances on different planes have been measured. Figure 6(a) shows the system at full immersion that is to say the small cylinder is fully immersed in the large tube. The

colour scheme of these charts indicate low permittivity regions as being blue and high permittivity regions as being red, however the corners of the square pixel grid are included in these reconstructed images and coloured blue. These pixels are present in all the cross-section slice tomograms however they are not representative of the circular sensor (in 2D-ECT these are typically removed from the image) and are therefore excised from all analyses.

The large tube is withdrawn from the ECT sensor at intervals of 1/8 penetration. It can be seen in Figure 6(b) that a reduction in the mean conductivity across the electrode plane occurs and continues through the other images within Figure 6 as the phantom moves through the sensor. The small cylinder is present inside the cylinder at all times even as the large tube is removed from the sensing zone. The first evidence of the presence of the small cylinder phantom is in Figure 6(e) where a series of voxels in the centre of the top cross-section planes of the 3D image register an increase in the permittivity. Moving from Figure 6(e) to Figure 6(h) it is clear this area of high permittivity spreads down the 3D tomograms in this series. This has to be attributed to the presence of the small cylinder in the centre of the sensor, however the shape of the high permittivity region is not clear which is unsurprising given the air gap between the cylinder and the sensor wall is 51 mm. The air gap affects the linearity assumption used in the sensitivity matrix. However, it is surprising that the small cylinder is affecting the inter-electrode electric field given the size of this air gap. The images given in Figure 6 have been smoothed to a high degree that gives the impression of soft edges in the process. To better represent the interface between low and high permittivity phases iso-surface plots of the same experiment imaged in the cross-section tomograms in Figure 6, are presented in Figure 7.
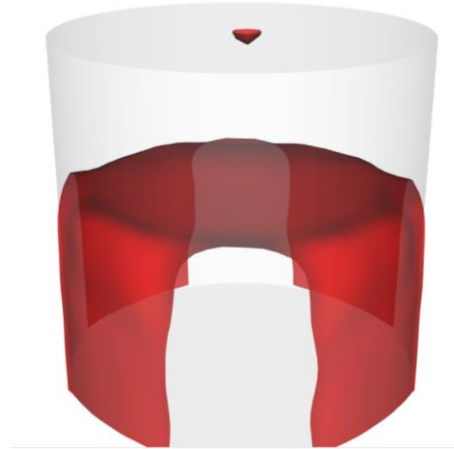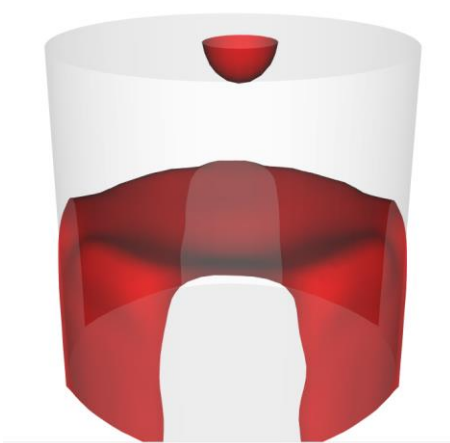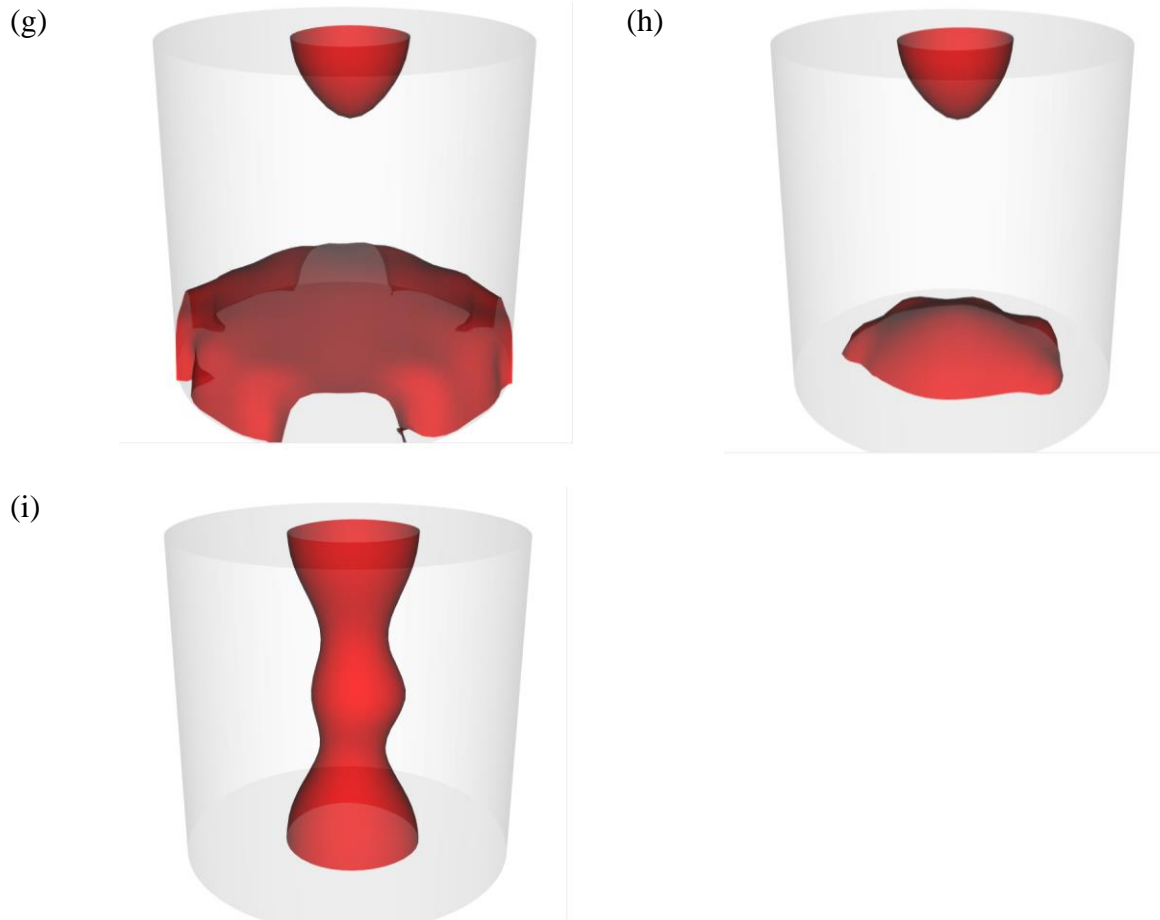
(g)

(h)

(i)

Figure 7 – Iso-surface plots of PE cylinder-in-tube phantoms, (a) Fully immersed large tube phantom, (b) 7/8 immersed, (c) ¾ immersed, (d) 5/8 immersed, (e) ½ immersed, (f) 3/8 immersed, (g) ¼ immersed, (h) 1/8 immersed, (i) Fully withdrawn

Iso-surface plots are calculated from volumetric data (given in Figure 6) and represent constant scalar data within a scalar 3D distribution. In the case of the phantom experiments this is represented as the interface between PE and air. Initially, in Figure 7(a), the sensor is at equivalent to high permittivity reference frame as the large tube is fully immersed in the sensor. The 4 rectangular regions at the sensor boundary are image artefacts and enclose the high permittivity region; they are able to be excised from the images but have remained to give clarity as regards to the phase distribution. Clearly as the PE large tube is removed from the sensor the interface is clearly shown to progress down the sensor. Figure 7(d) shows the

presence of the small cylinder at the top of the image, indicating that although the large tube was 5/8 immersed in the sensor and the small cylinder occupies the centre of the void behind the interface, it is not clearly detected by the sensor.

When the large tube reaches 1/4 immersed in Figure 7(g) the small tube is imaged as a rounded cone and the interface of the large tube and air is clearly present at the bottom of the sensor. The imaged shape of the small cylinder is consistent from Figure 7(e) to Figure 7(h) and is only imaged as a cylinder once the large tube is fully removed from the sensor in Figure 7(i). This result is symptomatic of a number of limitations of the technique in its current state: the limit of the software to drive a maximum of three planes, the reconstruction algorithm when imaging hard boundaries and the low permittivity ratio between the two phases ($\sigma_{air} = 1, \sigma_{PE} = 2.13$). ECT images the permittivity difference between phases therefore by keeping this difference high, the ability of the instrument to detect a hard boundary theoretically increases.

4.2. <u>Binary image refinement of 3D ECT Tomograms</u>

Following on from the evaluation of accuracy of 2D-ECT tomograms, a similar error analysis has been applied to the cylinder in tube experiment. The reference image for the voxel-by-voxel analysis has been shown above in Figure 5. The voxel values are extracted from the tomographic data and processed using MATLAB (MathWorks®). The voxel-by-voxel and the volumetric error are calculated for several values in the interval between 0.2 and 0.7 in order to evaluate the optimal value in terms of minimum error.

(a)

(b)
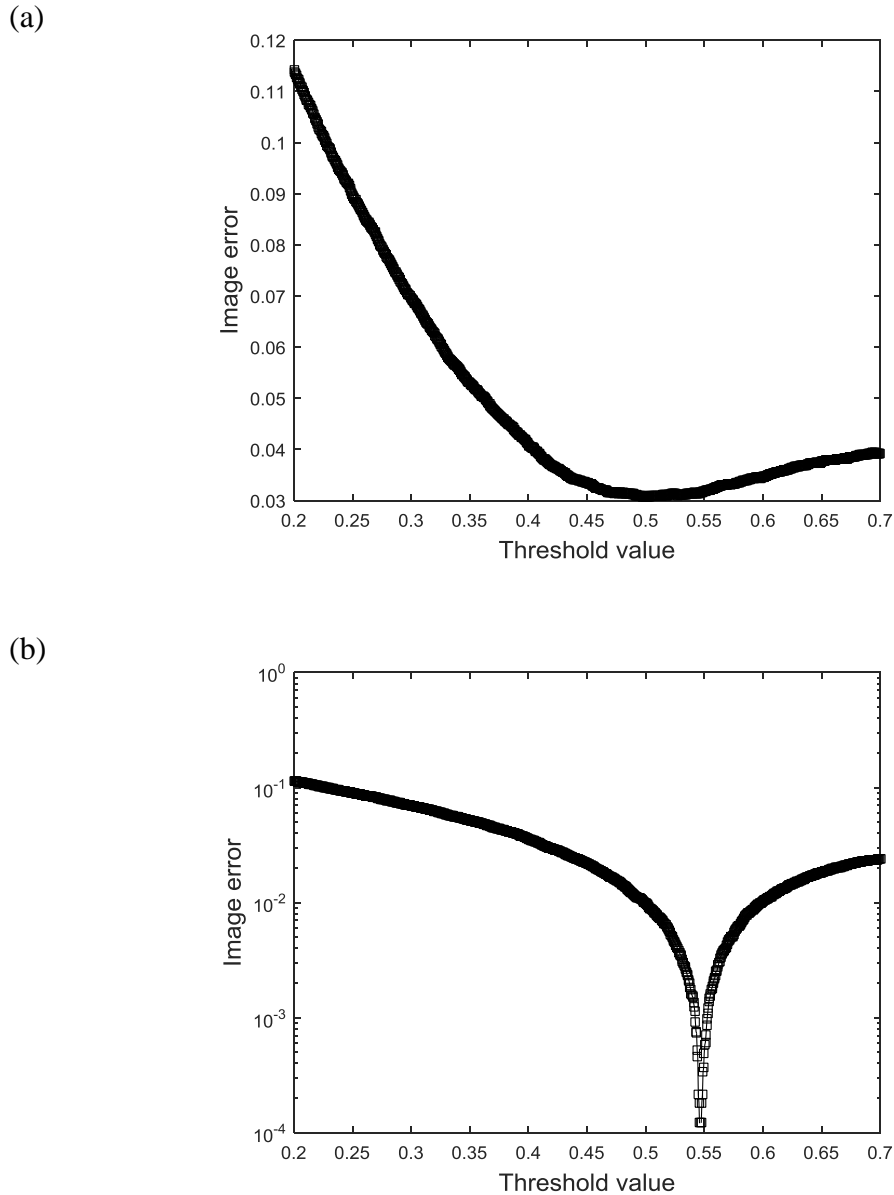
Figure 8 - Binary sensitivity to thresholds of 3D-ECT tomograms of PMMA cylinders (a) Voxel-by-Voxel error analysis, (b) Volumtric analysis

As shown in Figure 8 in both cases it is possible to reach very low errors and the optimum threshold value does not change substantially, it is 0.501 accordingly to the voxel-by-voxel analysis (Figure 8(a)) and 0.547 applying the volumetric analysis (Figure 8(b)). This characteristic is an important sign of robustness of the reconstruction and it allows to state that the results do not change substantially if it the threshold value is fixed applying

either error analysis methodology. In fact, if we use the voxel-by-voxel method to compare the error committed choosing the threshold value at the minimum of Figure 8(a) and Figure 8(b), the results are 0.0306 and 0.0316 respectively. This confirms the strength of the volumetric analysis which unlike the voxel-by-voxel analysis does not need the precise geometric information relative to the position of the phantom or objects within the sensor.

In Figure 9 the iso-surface plots display the reconstructed interface between the phantom and the gas phase using the threshold value suggested by the voxel-by-voxel (Figure 9(a)) and the volumetric (Figure 9(b)) analysis.

(a)
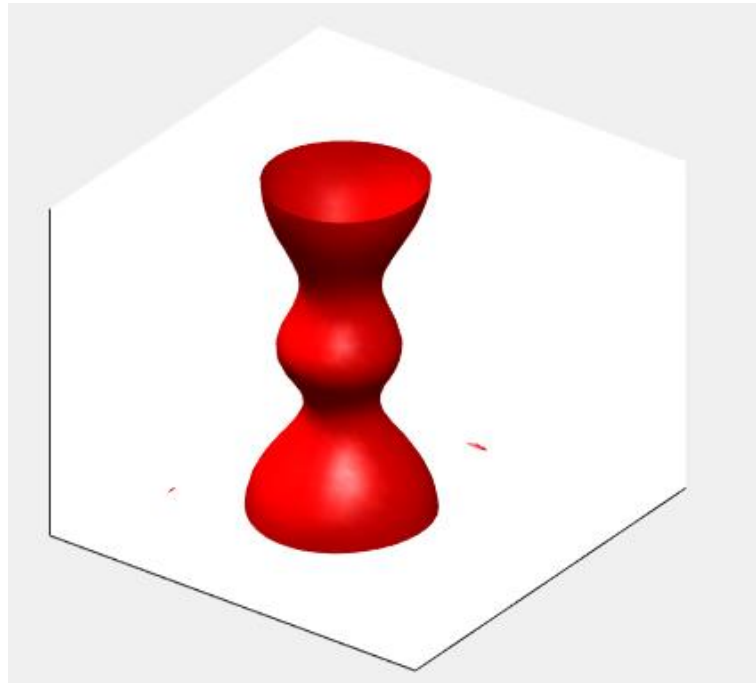
(b)
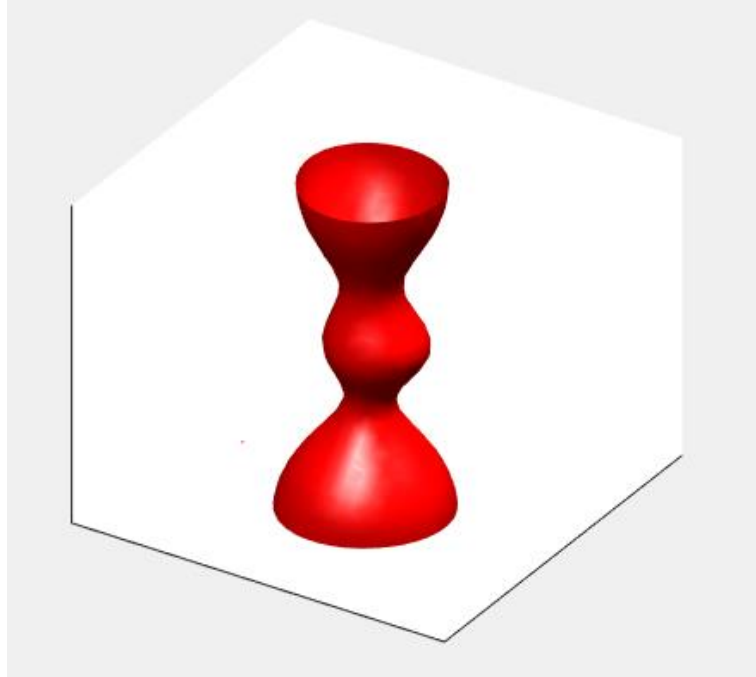
Figure 9 – 3D ECT iso-surface plots with applied optimal threshold value (a) Voxel-by-voxel threshold value = 0.501, (b) Volumetric threshold value = 0.547

The obtained images from both analyses are very similar with both unable to display a geometric cylindrical shape, a limitation of the spatial resolution provided by single-step reconstruction algorithms. The permittivity difference between the air and PE is approximately 2 thereby reducing the SNR of the measurement leading to lower image accuracy. The data post-processing improves the image accuracy as the images presented in Figure 9 more closely represent the cylindrical phantom than Figure 7(i). To reduce image error the two available options with the current ECT instrumentation is to use an alternative reconstruction algorithm or improve the phase permittivity difference.

5.0. *Conclusions*

This paper examines recent innovations in the field of 3D Electrical Capacitance Tomography and the application to 3D-ECT of previously used 2D-ECT post-processing methods that improve tomogram accuracy of imaged geometric phantoms. Firstly, development work of the data processing techniques applied to 2D-ECT is examined and shown to be effective, then using a similar phantom system the 3D-ECT method is used to acquire 3D tomograms and a similar analysis is adopted.

A series of phantom experiments were carried out that, using 3D-ECT, imaged a PE cylinder-in-tube phantom mimicking an interface moving through the sensor as the outer tube was withdrawn. The inner, small cylinder left in the centre of the sensor tested the sensitivity of the electrodes to very minor perturbations in the electric field where the measurement density is lowest. Cross-sectional 3D tomograms have been presented clearly showing the withdrawal of the large tube, these images were validated by using iso-surface images to show the location of the PE/air interface at penetration intervals on the small cylinder of 1/8 of the cylinder length.

As the fully withdrawn small PE cylinder is the only exact known geometry in this experiment this was used in the image error analysis using a thresholding approach, similar to that shown in 2D-ECT. A voxel-by-voxel approach has been compared with a volumetric approach demonstrating the robustness of the latter as it does not require precise geometric information to provide improved tomographic accuracy.

The data that have been presented show the real potential for commercialised 3D-ECT to provide *in-situ*, real time measurements of the sensing zone and the location of hard boundaries of these materials. The image accuracy is a function of the spatial resolution that is dependent upon both the software (reconstruction algorithm and data processing) and

hardware (electrodes/DAS) used in the measurement. When these are improved the results quality improves therefore making this method more applicable to chemical processes.

6.0. *Acknowledgements*

7.0. *References*

1. Peng L, Mou C, Yao D, Zhang B, Xiao D. Determination of the optimal axial length of the electrode in an electrical capacitance tomography sensor. *Flow Measurement and Instrumentation*. [Online] 2005;16(2-3): 169–175. Available from: doi:10.1016/j.flowmeasinst.2005.02.015 [Accessed: 1st June 2005]

2. Xu H, Yang G, Wang S. Effect of Axial Guard Electrodes on Sensing Field of Capacitance Tomographic Sensor. *Proceedings of WCIPT1*. Buxton, UK; 1999. p. 348–352.

3. Jaworski AJ, Bolton GT. The design of an electrical capacitance tomography sensor for use with media of high dielectric permittivity. *Measurement Science and Technology*. [Online] 2000;11(6): 743. Available from: doi:10.1088/0957-0233/11/6/318 [Accessed: 29th July 2015]

4. Hamidipour M, Larachi F. Characterizing the liquid dynamics in cocurrent gas-liquid flows in porous media using twin-plane electrical capacitance tomography. *Chemical Engineering Journal*. [Online] 2010;165(1): 310–323. Available from: doi:10.1016/j.cej.2010.08.058

5. Rimpilainen V, Heikkinen LM, Vauhkonen M. Moisture distribution and hydrodynamics of wet granules during fluidized-bed drying characterized with

volumetric electrical capacitance tomography. *Chemical Engineering Science*. [Online] 2012;75(0): 220–234. Available from: doi:10.1016/j.ces.2012.03.028

6. Warsito W, Fan LS. Neural network multi-criteria optimization image reconstruction technique (NN-MOIRT) for linear and non-linear process tomography. *Application of Neural Networks to Multiphase Reactors*. 2003;42(8–9): 663–674.

7. Warsito W, Fan LS. Development of 3-Dimensional Electrical Capacitance Tomography based on Neural Network Multi-Criterion Optimization Image Reconstruction. 2003. p. 391–396.

8. Warsito W, Fan LS. Dynamics of spiral bubble plume motion in the entrance region of bubble columns and three-phase fluidized beds using 3D ECT. *7th International Conference on Gas-Liquid and Gas-Liquid-Solid Reactor Engineering 7th International Conference on Gas-Liquid and Gas-Liquid-Solid Reactor Engineering*. 2005;60(22): 6073–6084.

9. Chandrasekera TC, Wang A, Holland DJ, Marashdeh Q, Pore M, Wang F, et al. A comparison of magnetic resonance imaging and electrical capacitance tomography: An air jet through a bed of particles. *Emerging Particle Technology*. 2012;227(0): 86–95.

10. Yang WQ, Peng L. Image reconstruction algorithms for electrical capacitance tomography. *Measurement Science and Technology*. 2003;14(1): R1–R13.

11. Clark PJ, Tsoligkas AN, Simmons MJH, Robbins PT, Stitt EH. A comparison of methods for in situ discrimination of imaged phase boundaries using electrical capacitance tomography. *Measurement Science and Technology*. [Online] 2016;27(2): 025401. Available from: doi:10.1088/0957-0233/27/2/025401 [Accessed: 9th February 2016]